Transport Signatures of Quasiparticle Poisoning in a Majorana Island

S. M. Albrecht,[1] E. B. Hansen,[1] A. P. Higginbotham,[1,2] F. Kuemmeth,[1] T. S. Jespersen,[1] J. Nygård,[1] P. Krogstrup,[1] J. Danon,[1,3] K. Flensberg,[1] and C. M. Marcus[1]

[1]*Center for Quantum Devices and Station Q Copenhagen, Niels Bohr Institute, University of Copenhagen, Copenhagen 2100, Denmark*
[2]*JILA, University of Colorado and NIST, Boulder, Colorado 80309, USA*
[3]*Department of Physics, NTNU, Norwegian University of Science and Technology, 7491 Trondheim, Norway*

(Received 17 December 2016; published 27 March 2017)

We investigate effects of quasiparticle poisoning in a Majorana island with strong tunnel coupling to normal-metal leads. In addition to the main Coulomb blockade diamonds, "shadow" diamonds appear, shifted by $1e$ in gate voltage, consistent with transport through an excited (poisoned) state of the island. Comparison to a simple model yields an estimate of parity lifetime for the strongly coupled island ($\sim 1\ \mu$s) and sets a bound for a weakly coupled island ($> 10\ \mu$s). Fluctuations in the gate-voltage spacing of Coulomb peaks at high field, reflecting Majorana hybridization, are enhanced by the reduced lever arm at strong coupling. When converted from gate voltage to energy units, fluctuations are consistent with previous measurements.

DOI: 10.1103/PhysRevLett.118.137701

Hybrid semiconductor-superconductor nanowire devices have been the focus of intense research in recent years [1–6] primarily because they are expected to support Majorana zero modes [7,8]. Of particular relevance to schemes for Majorana fusion-rule testing, braiding, and Majorana-based quantum computation [9–12] is the Majorana island geometry, in which the topological hybrid nanowire acquires a charging energy that lifts the degeneracy between occupied and empty Majorana states [6,13–16], allowing for charge readout of the state parity.

A fundamental bound to the coherence of Majorana based qubits is the parity lifetime of the Majorana state, limited by quasiparticle poisoning [9,17,18]. Studies on metallic superconductors have explored the associated poisoning rates in great detail [19–28], while experiments on semiconductor-superconductor hybrids have only established bounds on the relaxation rate of quasiparticles into the subgap state [29], with quantitative estimates for poisoning from external sources still pending.

In this Letter, we use Coulomb blockade spectroscopy to quantify the quasiparticle poisoning time of a Majorana island. We find the poisoning time to a state with one extra quasiparticle in the BCS continuum to be $\sim 1\ \mu$s in the regime of relatively strong coupling between the island and the leads, and bounded from below by $10\ \mu$s in the less strongly coupled regime investigated in Ref. [29]. Our results demonstrate transport signatures of quasiparticle poisoning in Majorana islands up to the topological phase transition and place constraints on a relevant time scale for topological quantum computation and Majorana braiding.

The device we investigate consisted of a MBE-grown [0001] wurtzite InAs nanowire with epitaxial Al on two of six facets [Fig. 1(a)], which induces a hard superconducing gap in the nanowire [30,31]. The Al shell was removed on both ends using a chemical etch, leaving an Al island of length $L \sim 400$ nm. Uncovered InAs segments at the wire ends are electrically contacted using normal-metal (Ti/Au) Ohmic contacts. Lithographically patterned electrostatic gates near the ~50 nm exposed segments next to the Ohmic contacts were used to deplete carriers, bringing the device into the Coulomb blockade regime. Magnetic fields were applied perpendicular to the nanowire axis, with out-of-plane field denoted $B_\perp$ and in-plane field denoted $B_{\rm tr}$ [Fig. 1(a), lower panel]. Because of the thin (~10 nm) Al

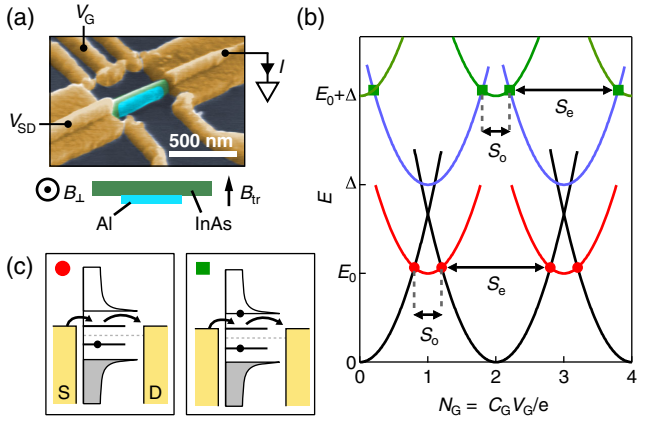

FIG. 1. (a) Top: Electron micrograph (false color) of a similar Majorana island device. The applied bias voltage $V_{\rm SD}$, gate voltage V_G, and measured current I are indicated. Bottom: Schematic top view (looking down onto the Si wafer) of the InAs nanowire (green) with two-facet epitaxial Al shell (light blue), showing the direction of applied magnetic fields $B_\perp$ and $B_{\rm tr}$. (b) Charge-state energies of the island as a function of gate induced charge N_G. Spacings between degeneracies indicated with S_e and S_o. (c) Schematics of transport processes for degeneracies indicated with red circles and green squares in (b).

shell on the side of the nanowire, superconductivity was preserved up to a large out-of-plane critical field, $B_{c,\perp} \sim 0.7$ T, and lower in-plane critical field, $B_{c,\mathrm{tr}} \sim 0.2$ T. The chemical potential of the island was controlled by the voltage V_G on a side gate. A voltage bias, V_{SD}, with 5 μV ac component at 314 Hz, was used to measure differential conductance using standard lock-in methods. All measurements were carried out in a dilution refrigerator with ~50 mK base temperature.

Before discussing experimental results, we briefly introduce a simple model of a hybrid Coulomb island with normal-metal leads (see Supplemental Material [32] for details). We take the density of states of the island to consist of a single subgap state at energy E_0 plus a Bardeen-Cooper-Schrieffer (BCS)-like continuum above a gap Δ [6,29]. For charging energy E_C exceeding thermal energy, the number of charges on the island N is well defined. We write $N = 2N_{\mathrm{cp}} + N_\Delta + N_0$, with N_{cp} the number of Cooper pairs on the island, $N_0 = 0, 1$ the occupation of the subgap state, and N_Δ the number of quasiparticles in the BCS continuum. Note that N_{cp} counts pairs of electrons, whereas N_Δ and N_0 count single electrons.

Neglecting thermal effects, we label the states in the Majorana island by their associated charge occupation numbers $(N_{\mathrm{cp}}, N_\Delta, N_0)$, with corresponding energies

$$E(N_{\mathrm{cp}}, N_\Delta, N_0) = \frac{E_C}{2}(N_G - N)^2 + N_\Delta \Delta + N_0 E_0, \qquad (1)$$

where $N_G = C_G V_G/e$ is the gate-induced charge on the island, C_G is the capacitance between island and side gate, and all quasiparticles in the BCS continuum are assumed to have relaxed to the gap energy, Δ. The resulting spectrum is show in Fig. 1(b) as a function of N_G (modulo an even integer), where we assume $E_0 < E_C/2 < \Delta$. For even N, the lowest available charge state (shown in black) is the pure condensate state $(N_{\mathrm{cp}}, 0, 0)$, followed by a state with an occupied subgap state and one quasiparticle in the BCS continuum $(N_{\mathrm{cp}}, 1, 1)$ (green). For odd N, the lowest two available charge states are $(N_{\mathrm{cp}}, 0, 1)$ and $(N_{\mathrm{cp}}, 1, 0)$, shown in red and blue.

At low temperatures and ignoring quasiparticle poisoning for now, the island is expected to be mostly in its ground charge state, with transport occurring only at charge-state degeneracies [red circles in Fig. 1(b)]. At these points, an extra electron can be added or removed from the island without energy cost, changing the occupation of the subgap state. Transport cycles at these degeneracies [left panel of Fig. 1(c)] correspond to the processes,

$$\begin{aligned} &(N_{\mathrm{cp}}, 0, 0) \rightleftarrows (N_{\mathrm{cp}}, 0, 1), \\ \text{and} \quad &(N_{\mathrm{cp}}, 0, 1) \rightleftarrows (N_{\mathrm{cp}} + 1, 0, 0). \end{aligned} \qquad (2)$$

The two degeneracies are symmetric about odd values of N_G, and produce a conductance peak pattern with unequal even and odd peak spacings, $S_e = \eta^{-1}(E_C + 2E_0)$ and $S_o = \eta^{-1}(E_C - 2E_0)$, where $\eta = e(C_G/C_{\mathrm{tot}})$ is the gate lever arm and $C_{\mathrm{tot}} = e^2/E_C$. The peak spacing difference, $S_e - S_o$, is thus proportional to E_0 [29] and can be used to track subgap states into the Majorana regime [6].

Quasiparticle poisoning excites the system from its charge ground state to a state with $N_\Delta = 1$ [green and blue parabolas in Fig. 1(b)]. Transport can now occur at charge-state degeneracies with $N_\Delta = 1$, marked as green squares in Fig. 1(b). The associated transport cycles [right panel of Fig. 1(c)] correspond to

$$\begin{aligned} &(N_{\mathrm{cp}}, 1, 0) \rightleftarrows (N_{\mathrm{cp}}, 1, 1), \\ \text{and} \quad &(N_{\mathrm{cp}}, 1, 1) \rightleftarrows (N_{\mathrm{cp}} + 1, 1, 0). \end{aligned} \qquad (3)$$

Processes that bring the island back to an unpoisoned state with $N_\Delta = 0$ include (i) Cooper pair recombination, $(N_{\mathrm{cp}}, 1, 1) \rightarrow (N_{\mathrm{cp}} + 1, 0, 0)$ (made possible by the lack of translational invariance), (ii) quasiparticle relaxation into the subgap state, $(N_{\mathrm{cp}}, 1, 0) \rightarrow (N_{\mathrm{cp}}, 0, 1)$, and (iii) quasiparticle tunneling out to a lead, $(N_{\mathrm{cp}}, 1, N_0) \rightarrow (N_{\mathrm{cp}}, 0, N_0)$. Depending on the relative magnitude of the corresponding relaxation rates, the poisoning rate, and the coupling of the subgap state to the source and drain leads $\Gamma_{S,D}$, the transport cycles in Eq. (3) can yield measurable conductance resonances. As evident from Fig. 1(b), the conductance peaks in the poisoned state should occur with the same peak spacings as the unpoisoned state, $S_{e,o}$, but shifted by $1e$ in gate voltage. The conductance height of the poisoned peaks contains quantitative information about the quasiparticle poisoning and relaxation rates.

Coulomb blockade spectroscopy of Majorana islands reported in Refs. [6,29] showed peaks at the unpoisoned resonances, Eq. (2), but no features associated with the poisoned transport cycles in Eq. (3). In the present experiment we use the 400 nm device from Ref. [6], with barriers set to be more transparent. This increases the rates $\Gamma_{S,D}$ as well as the rate of quasiparticle poisoning from the leads, giving rise to measurable transport features associated with the poisoned resonances (3). We have observed similar behavior in two devices and present results from one device here.

Figure 2(a) shows the differential conductance, $g = dI/dV_{\mathrm{SD}}$ as a function of V_{SD} and V_G at zero magnetic field. The data show a high-conductance Coulomb diamond pattern with large even-occupancy diamonds, small odd-occupancy diamonds, and negative differential conductance (NDC) at finite bias, similar to previous measurements [6,29]. The nearly vanishing odd diamond indicates that the subgap state energy E_0 is only slightly smaller than $E_C/2$ [6,29,35,36].

From the main Coulomb blockade diamonds we extract a charging energy $E_C = 210$ μeV, a gate lever arm $\eta = 2E_C/(\langle S_e \rangle + \langle S_o \rangle) = 6.2$ meV/V, and a zero-field

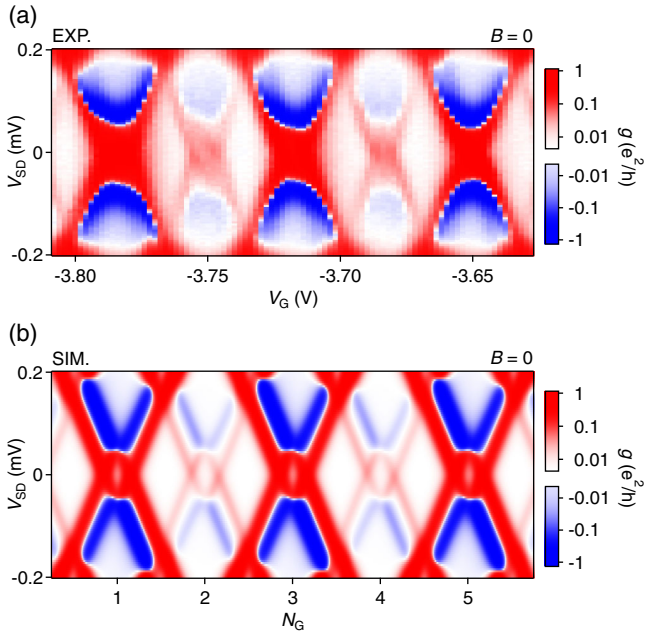

FIG. 2. (a) Experimental differential conductance g as a function of gate voltage, V_G, and source-drain voltage, V_{SD}, at zero magnetic field, showing a series of $2e$-periodic Coulomb diamonds with a second set of weaker shadow diamonds offset from the main diamonds by $1e$. (b) Numerically calculated differential conductance as a function of gate-induced charge N_G and source-drain voltage. See main text for model parameters.

subgap state energy $E_0 = 75\ \mu$eV. The width and magnitude of the conductance peak, taken at a magnetic field where peak overlap is minimal (see below), gives an asymmetric coupling of the subgap state to the source and drain leads which we fit as $\Gamma_S \sim 1$ and $\Gamma_D \sim 6$ GHz, significantly stronger than the coupling of ~0.5 GHz reported in Ref. [29].

Figure 2(a) shows in addition to the main Coulomb diamonds with peak conductance $g_m \sim 0.5\ e^2/\mathrm{h}$, a weaker set of "shadow" Coulomb diamonds centered on the valleys of the main diamonds, with peak conductance $g_s \sim 0.03\ e^2/\mathrm{h}$. The shadow diamonds are similar to the main diamonds, including regions of NDC, though much lower in conductance and shifted by the equivalent of $1e$ in gate voltage. Similar shadowlike peaks were previously investigated in metallic superconductor islands [37], in that case made visible by increasing temperature rather than island-lead coupling.

We attribute the shadow diamonds to quasiparticle poisoning, as in Ref. [37]. By comparing the main and shadow peak conductances to a rate-equation model of transport with poisoning, we extract a characteristic poisoning time, τ_p, associated with occupancy-changing excitations $(N_{\mathrm{cp}}, 0, N_0) \rightarrow (N_{\mathrm{cp}}, 1, N_0)$ (electronlike) and $(N_{\mathrm{cp}}, 0, N_0) \rightarrow (N_{\mathrm{cp}} - 1, 1, N_0)$ (holelike) in the BCS continuum. The model does not include poisoning events that populate the subgap state as they will tunnel out again on a time scale set by the large state-lead coupling, Γ_D, and thus not contribute significantly to the shadow peak conductance. In the limit of a weakly coupled island, τ_p sets a lower bound on the parity lifetime of the Majorana state.

Input to the model includes independently measured values for E_C, η, E_0, and $\Gamma_{S,D}$ (see Supplemental Material [32]). Additional parameters are the lead-continuum conductance, $g_{\mathrm{Al}} \sim 0.7\ e^2/\mathrm{h}$, measured from high-bias conductance data, the induced superconducting gap, $\Delta = 140\ \mu$eV, chosen to match the onset of NDC, and the relaxation time of quasiparticles from the continuum to the subgap state, previously measured to be $\tau_{\mathrm{qp}} = 0.1\ \mu$s in similar devices [29]. Simulated differential conductance g as a function of V_{SD} and N_G [Fig. 2(b)] reproduces the qualitative features of the experimental conductance data. A poisoning time of $\tau_p = 1.2\ \mu$s gives the best agreement with the observed ratio of main and shadow-peak conductance (see below for more details).

Figure 3(a) shows the measured zero-bias differential conductance as a function of V_G and perpendicular magnetic field $B_\perp$. The (initially small) odd Coulomb valley spacings S_o increase with $B_\perp$ up to a field of $B_\perp \sim 0.16$ T, where the average peak spacings become uniform, $\langle S_e \rangle = \langle S_o \rangle$, indicating a zero-energy state $E_0 = 0$. For higher fields, the peak spacings oscillate as a function of magnetic field, as expected theoretically for hybridized Majorana modes [13,38,39] and observed experimentally [6,16]. From the near-linear dependence on $B_\perp$ of the peak spacings at lower fields we extract an effective g factor of 16, large for InAs [40,41], but consistent with previous measurements on InAs nanowire Coulomb islands [6,16]. Shadow peaks have the same magnetic-field dependence as the main peaks, shifted by $1e$ gate-induced charge. Above $B_\perp \sim 0.16$ T, where $E_0 \sim 0$, main and shadow peaks merge.

The model includes the Zeeman effect by linearly lowering the subgap energy with magnetic field, $E_0 = 75\ \mu\mathrm{eV} - E_Z$, for $E_Z \leq 75\ \mu$eV. To model the topological phase transition at $E_Z = 75\ \mu$eV, we set $E_0 = 0$ for $E_Z > 75\ \mu$eV, neglecting Majorana mode hybridization. The resulting conductance g as a function of N_G and E_Z is shown in Fig. 3(b). Using $\tau_p = 1.2\ \mu$s from Fig. 2(b) reproduces the qualitative features of the data, including the splitting and merging of main and shadow peaks.

A cut of g vs V_G at $B_\perp = 50$ mT (where the overlap between adjacent peaks is minimal) is shown in Fig. 3(c). Defining g_m and g_s as the average main and shadow peak conductance, we find $g_m/g_s \sim 18$ in the presented gate range. Model conductance curves for different poisoning times are show in Fig. 3(d), showing an increase in g_s and decrease in g_m for decreasing τ_p. The decrease in g_m, deemphasized by the logarithmic scale in Fig. 3(d), matches the increase in g_s, reflecting that the Majorana island is either in a poisoned or in an unpoisoned state. For these parameters, the model yields the simple dependence,

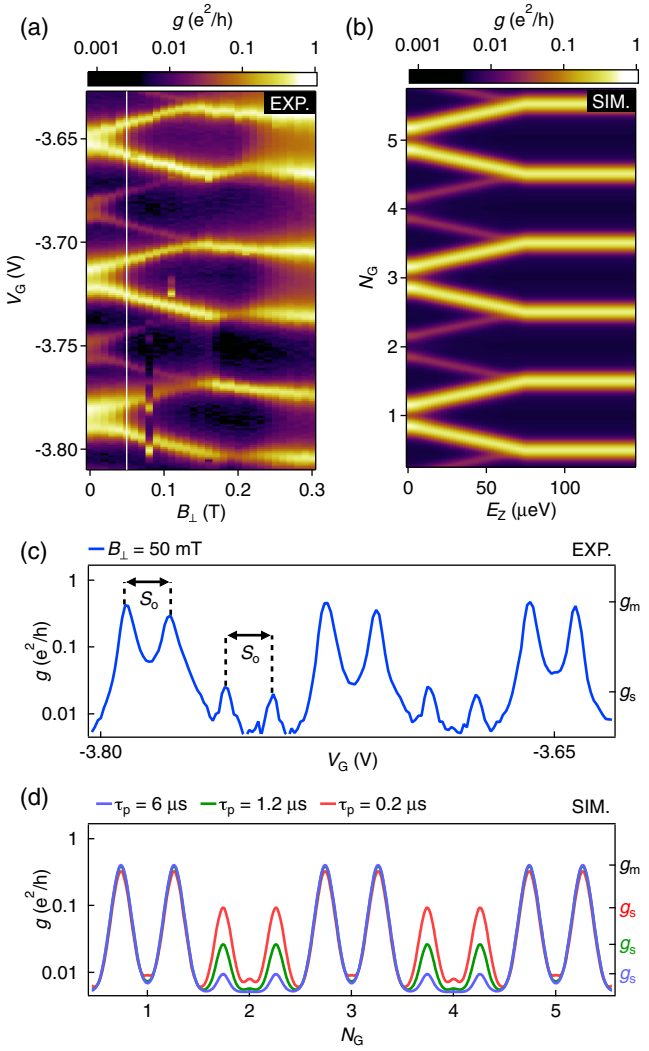

FIG. 3. (a) Measured zero-bias differential conductance g as a function of perpendicular magnetic field, $B_\perp$, and gate voltage, V_G, showing a series of strong even-odd Coulomb peaks with weaker shadow peaks in the even valleys between main peaks. Both sets of peaks split with increasing field and merge at $B_\perp \sim 0.16$ T. (b) Simulated differential conductance as a function of Zeeman energy, E_Z, and dimensionless gate voltage (charge number), N_G. (c) Measured differential conductance vs V_G at $B_\perp = 50$ mT [white line in (a)]. The average heights of the main and shadow peaks are indicated by g_m and g_s, respectively. (d) Simulated differential conductance as a function of N_G for poisoning times $\tau_p = 0.2$, 1.2, and 6 μs. Simulations show an increase in g_s and decrease in g_m for decreasing τ_p.

$\tau_p = a(g_m/g_s) + b$, with $a = 0.068$ and $b = -0.004$ μs. From this relation and the observed ratio g_m/g_s, we infer $\tau_p = 1.2 \pm 0.1$ μs.

The presented data are not taken in an optimal tuning for long parity lifetimes. By estimating the maximum ratio g_m/g_s from the noise floor in more weakly coupled device tunings, where no shadow diamonds were observed [6], we place a conservative estimate on the poisoning time of $\tau_p > 10$ μs. In the limit of a fully decoupled island this time scale of ~ 10 μs sets a conservative bound on the parity lifetime of the Majorana state.

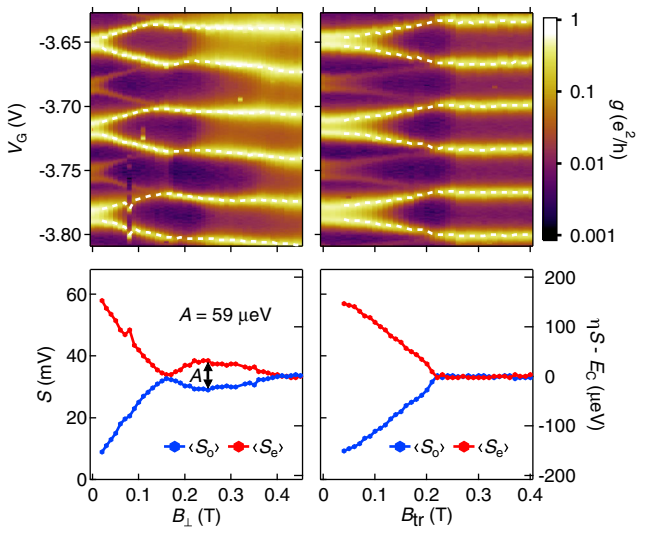

FIG. 4. Upper panels: Differential conductance g as a function V_G and magnetic fields perpendicular ($B_\perp$, left) and transversal (B_{tr}, right) to the nanowire. White dashed lines indicate the fitted peak positions. Lower panels: Extracted average peak spacing for even and odd Coulomb valleys, $\langle S_{e,o} \rangle$, as a function of magnetic field. The left axis has units of gate voltage, the right axis shows the associated energy scale $\eta S - E_C \propto E_0$.

Finally, we investigate the behavior of the main and shadow peaks for different magnetic field directions. The magnetic-field dependent splitting is compared for directions $B_\perp$ and B_{tr} in Fig. 4. In both cases, the estimated peak center, indicated by a dashed white line in the upper panels of Fig. 4, is used to calculate average Coulomb peak spacings for the two even and the three odd valleys of the main set of Coulomb peaks, denoted $\langle S_e \rangle$ and $\langle S_o \rangle$. The result is shown in the lower panels of Fig. 4, where the right axis indicates the energy scale for the lowest subgap state $\eta S - E_C \propto E_0$. The shadow peak is not used in this analysis as it cannot be distinguished from the main peak for higher fields.

For increasing perpendicular field $B_\perp$ (left panels in Fig. 4), $\langle S_e \rangle$ and $\langle S_o \rangle$ become equal at $B_\perp \sim 0.16$ T, indicating the emergence of a state at $E_0 = 0$, and subsequently oscillate in magnetic field. The amplitude of these oscillations, $A = 59$ μeV, is close to the expected value for hybridized Majorana modes in a device with $L = 400$ nm: We estimate $A = A_0 e^{-L/\xi} = 64$ μeV, based on previous fits of the constants $A_0 = 300$ μeV and $\xi = 260$ nm [6]. We stress that data from the same device as we use here but measured in a different tuning (without shadow peaks), was included in the original analysis to determine A_0 and ξ [6].

For increasing in-plane fields B_{tr} (right panels in Fig. 4), the shadow peaks again split, similar to the main peaks, and acquire a $1e$-periodic spacing at $B_{tr} = 0.22$ T, with no

oscillations visible for higher fields. Independent measurements show a closing of the superconducting gap for this device at $B_{c,tr} = 0.25$ T, suggesting that the transition to $1e$-periodic peak spacings is in this case caused by destruction of superconductivity. We note the different curvatures of $\langle S_{e,o}\rangle$ as they approach the field where $\langle S_e\rangle = \langle S_o\rangle$: $\langle S_{e,o}\rangle$ bends outwards for $B_\perp$ and inwards for $B_{\rm tr}$. Since $\eta\langle S_e\rangle - E_C \propto E_0$ and $\eta\langle S_o\rangle - E_C \propto -E_0$, the outward bending behavior for $B_\perp$ suggests subgap states approaching the topological phase transition [38,39,42], whereas the inward bending for increasing $B_{\rm tr}$ suggests a subgap state energy following a quadratically closing induced superconducting gap.

In conclusion, we have observed and modeled shadow diamonds offset from the main Coulomb diamonds by $1e$, associated with quasiparticle poisoning of a Majorana island, yielding estimates for poisoning times on a $\sim 1\ \mu$s time scale. High-field measurements indicate a transition to the topological phase, with extracted Majorana mode hybridization energies consistent with previous measurements.

We thank Roman Lutchyn, Leonid Glazman, and Mingtang Deng for valuable conversations. Research supported by Microsoft, the Danish National Research Foundation, the Lundbeck Foundation, Carlsberg Foundation, Villum Foundation, and the European Commission.

[1] V. Mourik, K. Zuo, S. M. Frolov, S. R. Plissard, E. Bakkers, and L. P. Kouwenhoven, Science **336**, 1003 (2012).
[2] L. P. Rokhinson, X. Liu, and J. K. Furdyna, Nat. Phys. **8**, 795 (2012).
[3] A. Das, Y. Ronen, Y. Most, Y. Oreg, M. Heiblum, and H. Shtrikman, Nat. Phys. **8**, 887 (2012).
[4] M. T. Deng, C. L. Yu, G. Y. Huang, M. Larsson, P. Caroff, and H. Q. Xu, Nano Lett. **12**, 6414 (2012).
[5] H. O. H. Churchill, V. Fatemi, K. Grove-Rasmussen, M. T. Deng, P. Caroff, H. Q. Xu, and C. M. Marcus, Phys. Rev. B **87**, 241401 (2013).
[6] S. M. Albrecht, A. P. Higginbotham, M. Madsen, F. Kuemmeth, T. S. Jespersen, J. Nygård, P. Krogstrup, and C. M. Marcus, Nature (London) **531**, 206 (2016).
[7] R. M. Lutchyn, J. D. Sau, and S. Das Sarma, Phys. Rev. Lett. **105**, 077001 (2010).
[8] Y. Oreg, G. Refael, and F. von Oppen, Phys. Rev. Lett. **105**, 177002 (2010).
[9] D. Aasen, M. Hell, R. V. Mishmash, A. Higginbotham, J. Danon, M. Leijnse, T. S. Jespersen, J. A. Folk, C. M. Marcus, K. Flensberg, and J. Alicea, Phys. Rev. X **6**, 031016 (2016).
[10] S. Vijay and L. Fu, Phys. Rev. B **94**, 235446 (2016).
[11] L. A. Landau, S. Plugge, E. Sela, A. Altland, S. M. Albrecht, and R. Egger, Phys. Rev. Lett. **116**, 050501 (2016).
[12] B. van Heck, A. R. Akhmerov, F. Hassler, M. Burrello, and C. W. J. Beenakker, New J. Phys. **14**, 035019 (2012).
[13] L. Fu, Phys. Rev. Lett. **104**, 056402 (2010).
[14] R. Hützen, A. Zazunov, B. Braunecker, A. L. Yeyati, and R. Egger, Phys. Rev. Lett. **109**, 166403 (2012).
[15] B. van Heck, R. M. Lutchyn, and L. I. Glazman, Phys. Rev. B **93**, 235431 (2016).
[16] D. Sherman, J. S. Yodh, S. M. Albrecht, J. Nygård, P. Krogstrup, and C. M. Marcus, Nat. Nanotechnology **12**, 212 (2017).
[17] D. Rainis and D. Loss, Phys. Rev. B **85**, 174533 (2012).
[18] M. Cheng, R. M. Lutchyn, and S. Das Sarma, Phys. Rev. B **85**, 165124 (2012).
[19] J. Aumentado, M. W. Keller, J. M. Martinis, and M. H. Devoret, Phys. Rev. Lett. **92**, 066802 (2004).
[20] A. J. Ferguson, N. A. Court, F. E. Hudson, and R. G. Clark, Phys. Rev. Lett. **97**, 106603 (2006).
[21] J. M. Martinis, M. Ansmann, and J. Aumentado, Phys. Rev. Lett. **103**, 097002 (2009).
[22] P. J. de Visser, J. J. A. Baselmans, P. Diener, S. J. C. Yates, A. Endo, and T. M. Klapwijk, Phys. Rev. Lett. **106**, 167004 (2011).
[23] M. Zgirski, L. Bretheau, Q. Le Masne, H. Pothier, D. Esteve, and C. Urbina, Phys. Rev. Lett. **106**, 257003 (2011).
[24] L. Sun *et al.*, Phys. Rev. Lett. **108**, 230509 (2012).
[25] D. Ristè, C. C. Bultink, M. J. Tiggelman, R. N. Schouten, K. W. Lehnert, and L. DiCarlo, Nat. Commun. **4**, 1913 (2013).
[26] V. F. Maisi, S. V. Lotkhov, A. Kemppinen, A. Heimes, J. T. Muhonen, and J. P. Pekola, Phys. Rev. Lett. **111**, 147001 (2013).
[27] I. M. Pop, K. Geerlings, G. Catelani, R. J. Schoelkopf, L. I. Glazman, and M. H. Devoret, Nature (London) **508**, 369 (2014).
[28] D. J. van Woerkom, A. Geresdi, and L. P. Kouwenhoven, Nat. Phys. **11**, 547 (2015).
[29] A. P. Higginbotham, S. M. Albrecht, G. Kirsanskas, W. Chang, F. Kuemmeth, P. Krogstrup, T. S. Jespersen, J. Nygård, K. Flensberg, and C. M. Marcus, Nat. Phys. **11**, 1017 (2015).
[30] P. Krogstrup, N. L. B. Ziino, W. Chang, S. M. Albrecht, M. H. Madsen, E. Johnson, J. Nygård, C. M. Marcus, and T. S. Jespersen, Nat. Mater. **14**, 400 (2015).
[31] W. Chang, S. M. Albrecht, T. S. Jespersen, F. Kuemmeth, P. Krogstrup, J. Nygård, and C. M. Marcus, Nat. Nanotechnol. **10**, 232 (2015).
[32] See Supplemental Material at http://link.aps.org/supplemental/10.1103/PhysRevLett.118.137701 for details on the rate-equation model, which includes Refs. [33,34].
[33] F. W. J. Hekking, L. I. Glazman, K. A. Matveev, and R. I. Shekhter, Phys. Rev. Lett. **70**, 4138 (1993).
[34] H. I. Jørgensen, T. Novotný, K. Grove-Rasmussen, K. Flensberg, and P. E. Lindelof, Nano Lett. **7**, 2441 (2007).
[35] M. T. Tuominen, J. M. Hergenrother, T. S. Tighe, and M. Tinkham, Phys. Rev. Lett. **69**, 1997 (1992).
[36] P. Lafarge, P. Joyez, D. Esteve, C. Urbina, and M. H. Devoret, Phys. Rev. Lett. **70**, 994 (1993).
[37] J. M. Hergenrother, M. T. Tuominen, and M. Tinkham, Phys. Rev. Lett. **72**, 1742 (1994).
[38] S. Das Sarma, J. D. Sau, and T. D. Stanescu, Phys. Rev. B **86**, 220506 (2012).

[39] T. D. Stanescu, R. M. Lutchyn, and S. Das Sarma, Phys. Rev. B **87**, 094518 (2013).
[40] M. T. Björk, A. Fuhrer, A. E. Hansen, M. W. Larsson, L. E. Fröberg, and L. Samuelson, Phys. Rev. B **72**, 201307 (2005).
[41] S. Csonka, L. Hofstetter, F. Freitag, S. Oberholzer, C. Schoenenberger, T. S. Jespersen, M. Aagesen, and J. Nygård, Nano Lett. **8**, 3932 (2008).
[42] D. Rainis, L. Trifunovic, J. Klinovaja, and D. Loss, Phys. Rev. B **87**, 024515 (2013).